Statistical Analyses of Satellite Cloud Object Data from CERES. Part II: Tropical Convective Cloud Objects During 1998 El Niño and Validation of the Fixed Anvil Temperature Hypothesis

Kuan-Man Xu[1], Takmeng Wong[1], Bruce A. Wielicki[1],

Lindsay Parker[2], Bing Lin[1], Zachary A. Eitzen[1,2], and Mark Branson[3]

[1]NASA Langley Research Center, Hampton, VA

[2]Science Applications International Corporation, Hampton, VA

[3]Colorado State University, Fort Collins, CO

Corresponding author address:

Dr. Kuan-Man Xu

Climate Science Branch

NASA Langley Research Center

Mail Stop 420

Hampton, VA 23681

e-mail: Kuan-Man.Xu@nasa.gov

Abstract

Characteristics of tropical deep convective cloud objects observed over the tropical Pacific during January-August 1998 are examined using the Tropical Rainfall Measuring Mission/Clouds and the Earth's Radiant Energy System single scanner footprint (SSF) data. These characteristics include the frequencies of occurrence and statistical distributions of cloud physical properties. Their variations with cloud-object size, sea surface temperature (SST), and satellite precessing cycle are analyzed in detail. A cloud object is defined as a contiguous patch of the Earth composed of satellite footprints within a single dominant cloud-system type.

It is found that statistical distributions of cloud physical properties are significantly different among three size categories of cloud objects with equivalent diameters of 100 - 150 km (small), 150 - 300 km (medium), and > 300 km (large), respectively, except for the distributions of ice particle size. The distributions for the larger-size category of cloud objects are more skewed towards high SSTs, high cloud tops, low cloud-top temperature, large ice water path, high cloud optical depth, low outgoing longwave (LW) radiation, and high albedo than the smaller-size category. As SST varied from one satellite precessing cycle to another, the changes in macrophysical properties of cloud objects over the entire tropical Pacific were small for the large-size category of cloud objects, relative to those of the small- and medium-size categories. This result suggests that the fixed anvil temperature hypothesis of Hartmann and Larson may be valid for the large-size category. Combining with the result that a higher percentage of the large-size category of cloud objects occurs during higher SST subperiods, this implies that macrophysical properties of cloud objects would be less sensitive to further warming of the climate. On the other hand, when cloud objects are classified according to SSTs where large-scale dynamics plays important roles, statistical characteristics of cloud microphysical properties, optical depth and albedo are not sensitive to the SST, but those of cloud macrophysical properties are strongly dependent upon the SST. Frequency distributions of vertical velocity from the European Center for Medium-range Weather Forecasts model that is matched to each cloud object are used to interpret some of the findings in this study.

1. Introduction

Climate model simulations are usually validated against gridded monthly-mean satellite observations. Numerical weather forecasts are validated against surface and upper-air observations, at least, at the daily time-scale. In both types of validations, the gridded data are used. They represent averages of physical parameters over an area of hundreds of kilometers in a horizontal direction. In the validation of climate model simulations, monthly-mean gridded satellite data may include many different types of cloud systems, due to changes in large-scale dynamic and thermodynamic environments. While these monthly-averaged satellite data are useful in some climate applications, they do not sufficiently constrain critical assumptions about the treatment of subgrid-scale processes and thus are generally not suitable to fully explore the direct cause of model deficiencies or to directly improve climate model parameterizations. Even when such data are carefully examined against model simulations, the models may perform well for the wrong reasons due to cancellation of errors in the monthly-averaged model output.

Xu et al. (2005; hereafter Part I) recently proposed a new methodology to analyze statistical properties of cloud systems from Earth Observing System (EOS) satellites in order to more rigorously validate model simulations. This is termed the "cloud object" approach. This approach identifies a cloud object as a contiguous patch of the Earth composed of satellite footprints within a single dominant cloud-system type. Satellite footprints are better known as "fields of view (fovs)." The shape and size of a cloud object are determined by the satellite footprint data and by the selection criteria based upon cloud physical properties for a given cloud-system type. For example, deep convective cloud objects are identified with footprints that have a cloud optical depth (τ) greater than 10, cloud top height greater than 10 km and cloud fraction of 100%. No arbitrary grid cell of the Earth is used in this new methodology. It is therefore *not* an Eulerian approach as in the monthly-averaged satellite data.

A broader application of this cloud-object approach is to integrate observational data analysis and high-resolution numerical modeling to improve the understanding of cloud feedbacks (Fig. 1). On the observational side, satellite data are first analyzed to generate large ensembles of

cloud objects for different cloud-system types to reach climate accuracy (Ohring et al. 2005). Statistical properties of cloud objects are analyzed in terms of the summary probability density functions (pdfs) or histograms over an ensemble of cloud objects (i.e., the combined pdfs of individual cloud objects). Second, the atmospheric state is matched to the time and location of each cloud object in such a way to allow for stratification of observed cloud objects according to some independent measures of the atmospheric states. This is needed to derive the partial derivatives of cloud properties versus atmospheric states, thus cloud feedbacks. These atmospheric states can be represented by the vertical velocity at 500 hPa for tropical deep convective cloud objects or the static stability in the lower troposphere for boundary-layer cloud objects.

On the numerical modeling side, the cloud-object matched atmospheric states such as the advective tendencies can be used to drive the simulations of high-resolution cloud models such as cloud resolving models (CRMs). A detailed description of the procedure is as follows. First, the statistics of the simulated cloud objects can be rigorously compared with those of satellite observations for large ensembles of cloud objects so that systematic errors can be identified and further improvements to the high-resolution cloud models can be made without the need for model tuning. This is called a "large ensemble model test," in contrast to tests that use data from a few field experiments (e.g., Xu and Randall 1996, 2000). Second, simulated cloud feedbacks can be analyzed and compared with those from satellite cloud-object analysis to further improve the high-resolution cloud models (Eitzen and Xu 2005). Third, further testing of the improved cloud models can be performed by embedding them into a global climate model for selected seasonal and interannual simulations. This revolutionary method of climate modeling is called the "multiscale modeling framework" (MMF; Randall et al. 2003). Finally, once the MMF passes these tests through extensive comparisons with both the observed frequencies of occurrence and statistical properties of cloud object types, decadal climate prediction can be performed to provide a more accurate prediction of climate change than that obtained using a conventional climate model.

Another application of this cloud-object approach, which will be explored in the present study, is to use the data to validate hypotheses for climate change. There are several hypotheses

regarding tropical climate change which postulate that relationships exist between radiative properties of clouds and sea surface temperatures (SSTs). Ramanathan and Collins (1991) analyzed the monthly-mean Earth Radiation Budget Experiment (ERBE) data and proposed a cirrus-cloud thermostat hypothesis. This hypothesis suggested that the high albedos of tropical deep convective clouds can limit the upper bound on the SST. Lindzen et al. (2001) proposed an adaptive iris hypothesis, in which the tropical upper-tropospheric anvils act as a strong negative feedback on the global climate system. Both hypotheses have been disputed by many studies (e.g., Lau et al. 1994; Hartmann and Michelsen 1993, 2002; Lin et al. 2002, 2005; Fu et al. 2002). For both hypotheses, the radiative feedback of clouds on the energy balance is directly related to the change of SST without considering the large-scale circulations that result from the meridional gradient of the SST (e.g., Hartmann and Michelsen 1993; Larson and Hartmann 2003b).

It is well known that the subsidence region of the Tropics is required to close the mass budget and the decrease of albedos in the subsidence region can cancel out the albedo increases over convective regions as the mean SST increases in the Tropics. This means that there exists an approximate heat balance in the tropical troposphere between the radiative cooling in the subsidence region and convective heating by latent heat release in the convective regions. Hartmann and Larson (2002) proposed the fixed anvil temperature (FAT) hypothesis in which the emission temperature at the top of convective anvil clouds in the Tropics will remain constant during climate change. They based this on the fact that the radiative cooling at the top of convective anvil clouds is determined by the emission temperature due to inefficient radiative emission from water vapor through the Clausis-Clapeyron relationship. This hypothesis was supported by mesoscale numerical model simulations (Larson and Hartmann 2003a, b), but it has not been validated by observational data. The use of cloud object data represents the first attempt to observationally validate this hypothesis.

In this part of the study, statistical characteristics of tropical convective cloud objects (hereafter, "cloud objects") will be analyzed from January-August 1998 of TRMM/CERES (Tropical Rainfall Measuring Mission/Clouds and the Earth's Radiant Energy System) data

period. This period corresponds to the mature and dissipative phases of the 1997/1998 El Niño. The objectives of this study are threefold: 1) to contrast the differences among three size categories of cloud objects, 2) to explore the relationships of the statistical properties of cloud objects with atmospheric state variables such as sea surface temperature (SST) and vertical velocity, and 3) to validate the FAT hypothesis of Hartmann and Larson (2002). Part I of this study presented some preliminary results from the analysis of the statistical properties of cloud objects associated with the strong 1997/98 El Niño in March 1998 and the very weak 2000 La Niña in March 2000. The present part extends the analysis of Part I to a longer period and to a greater depth.

Section 2 briefly describes satellite and the matched atmospheric state data and methodology. Results for the variations of cloud-object characteristics with size, SST and satellite precessing cycle are presented in Sections 3, 4 and 5, respectively. Conclusions and discussion are given in Section 6. The cloud object data are available from the web: http://cloud-object.larc.nasa.gov/.

2. Data and methodology

2a. Cloud object data

The details of cloud object methodology and the data used in generating the cloud object data product are presented in Part I. Briefly, the basic data with which the cloud object data are produced are a level-2 CERES Single Scanner Footprint (SSF) top-of-atmosphere (TOA)/Surface Fluxes and Clouds data product (Wielicki et al. 1996). The cloud-object data product contains cloud optical, microphysical and macrophysical properties, and broadband TOA reflected shortwave (SW) and emitted longwave (LW) fluxes from the CERES instrument. The full list of these parameters is given in Table 1 of Part I. The CERES broadband radiative fluxes are produced using the new generation of angular distribution models derived from the TRMM CERES broadband radiance observations (Loeb et al. 2003). Scene identification (type and clear/cloudy) and cloud properties (i.e., cloud effective height, temperature, pressure, particle types and equivalent diameters) are retrieved from the high-resolution cloud imager, the Visible Infrared Scanner (VIRS), on the TRMM satellite. These data have been averaged over the larger CERES instru-

ment footprints to produce an integrated and radiation-constrained cloud and radiation data set. Details of the retrieval methods are described in Minnis et al. (1997).

2b. Cloud object methodology

A cloud object is defined as a contiguous patch composed of CERES footprints that satisfy a set of physically-based cloud-system selection criteria. A "region-growing" strategy based on imager-derived cloud properties is used to identify the cloud objects within a single satellite swath (Wielicki and Welch 1986). For all CERES fovs in a 700 km wide TRMM swath, each CERES fov that meets the selection criteria is marked as part of a cloud object. These "seed points" are grown using the algorithm described in Wielicki and Welch (1986). Only fields of view that are adjacent and that meet the selection criteria of a single cloud type can be joined in a cloud object. By adjacent, we mean CERES fovs that are next to each other along the scanning direction, or perpendicular to it. Cloud objects are uniquely determined when they share no adjacent CERES fovs. Cloud objects that grow to an equivalent diameter of less than 100 km, approximately 75 fovs, are ignored in the present analysis to limit data noise.

The selection criteria for the tropical deep convective cloud-object type, as mentioned in Section 1, are composed of both cloud top height and τ because we are interested in thick, upper tropospheric anvils and cumulonimbus towers in the tropical region. The cloud top height must be greater than 10 km and τ must be greater than 10. The cloud fraction of the footprint must be 100%. Furthermore, all fovs must be located within the Pacific Ocean between 25 °S and 25 °N.

In the present study, eight months (January-August 1998) of the TRMM CERES data are analyzed. These eight months correspond to the peak and dissipative phases of the 1997/1998 El Niño (Cess et al. 2001). In the analyses presented below, satellite cloud object data for this period are then sorted either by the size of cloud objects as measured by their equivalent diameter, or by the (cloud-object) mean SST, or by the satellite precessing cycle. The TRMM 46-day precessing cycle gives a complete sampling of the diurnal cycle at a given location, i.e., to avoid diurnal aliasing issues. In all analyses, both the frequencies of occurrence of cloud objects and the statisti-

cal distributions of cloud physical properties will be examined, as well as the frequency distributions of vertical velocity from the European Center for Medium-range Weather Forecasts (ECMWF) model that is matched to each cloud object.

2c. Matched ECMWF data

The ECMWF analyses over the Tropics are available on 0.5625° x 0.5625° grid meshes every six hours from its data assimilation system. The data include horizontal wind components, temperature and water vapor profiles, etc. However, the vertical velocity (in pressure coordinate, ω) was not available from the ECMWF analyses. In this study, vertical velocity and advective heat and moisture tendencies are actually calculated by the Colorado State University general circulation model (GCM). The GCM is run for a single time step with initial input data from ECMWF. Details of this procedure can be found in Eitzen and Xu (2005). These tendencies are used to drive CRM simulations after they are matched to the time and location of the observed cloud objects. The gap in time matching is less than three hours. In matching the location of the cloud object, a rectangular box (latitude x longitude) is drawn to cover the four outermost corner footprints of the cloud object; i.e., parts of the environment surrounding the cloud objects are included. If one side of this box is larger than 7.3125° in length (13 grid cells), a maximum length of 7.3125° centered near the center of the cloud object is used, instead. This happens for a few very large cloud objects or irregularly shaped cloud objects. Then, every grid cell within the rectangular box will be used to calculate the frequency distributions of vertical velocity as a function of pressure, as shown in Sections 3, 4 and 5.

It is well known that large-scale advective tendencies of heat and moisture are closely linked to the intensity of convective cloud systems. Because horizontal advective tendencies in the Tropics are usually small, compared to their vertical counterparts, vertical velocity can be used as an indicator of the intensity of tropical deep convection. For example, Bony et al. (2003) sorted the monthly-mean TOA longwave and shortwave cloud radiative forcings at 4° x 5° grid cells according to the similarly averaged ω at 500 hPa (hereafter, ω_{500}). The frequency distribu-

tion of ω_{500} in the current study shown later in the paper, however, have different characteristics because these vertical velocities are the instantaneous values at a much smaller grid-cell size (0.5625° x 0.5625°). In particular, the magnitudes can be one or two orders larger than those of the monthly-mean vertical velocity. Because of this instantaneousness, the frequency distributions of vertical velocity at a single level may not be able to characterize the different dynamic environments of cloud objects associated with different size categories, SST ranges or precessing cycles. To overcome this problem, the frequency distributions of vertical velocity are first calculated as a function of pressure for every size category. These frequency distributions are then used to calculate the frequency departures for subsets of cloud objects classified according to SST or satellite precessing cycle.

3. Variations of cloud object characteristics with size

3a. Frequency of occurrence

The cloud objects identified from the CERES SSF data are tabulated according to the range of their equivalent diameters. Three size categories are considered. They are defined by the ranges of 100 - 150 km (small size), 150 - 300 km (medium size) and greater than 300 km (large size). For convenience, they are termed the S, M and L size categories, respectively. The total number of cloud objects for the S, M and L categories is 858, 899 and 500, respectively, for these eight months of CERES data. Although the S and M size categories of cloud objects occur more frequently than the L size category, the total numbers of CERES footprints for the L size category are much greater, 65.4% of the sum of all three size categories, than the S and M size categories, due to the much larger mean number of footprints for the L size cloud objects. The numbers of CERES footprints also vary from one cloud object to another within each size category. Table 1 shows the statistics of the footprint numbers for the S, M and L size categories. The intra-category variability is large for the L size category because the equivalent radii range from 300 km to 900 km in this size category.

3b. Statistical properties of cloud objects

Figure 2 shows summary histograms of seven cloud, optical and radiative properties, as well as SST, for all three size categories. These summary histograms are constructed by utilizing all 97700, 309000 and 767300 footprints for the S, M and L size categories, respectively. The probability density is the number of footprints within a bin interval divided by the total number of footprints of a size category and the bin size. There are significant differences among the three size categories for all summary histograms of cloud and radiative properties, except for those of ice particle size between the S and M size categories and between the S and L size categories, despite the relatively small differences in their SST histograms (Fig. 2a). This suggests that the SST is not the primary cause for the differences in cloud, optical and radiative properties among the three size categories, especially between the S and M size categories.

The differences in the SST distributions between the S and M size categories are not statistically significant, according to a statistical significance test based on the bootstrap method (Efron and Tibshirani 1993). The detailed procedure for this test was presented in Xu (2005). Table 2 shows the statistical significance level (p) or p-value. The threshold p-value is customarily chosen to be 0.05. When the p-value is less than 0.05, there is a small probability that two summary histograms are not different. For example, the statistical significance test shows that the differences in SST between the S and M size categories are statistically insignificant with a p-value much greater than 0.05. The L size cloud objects occur more frequently over relatively warmer SSTs, in particular, over SSTs between 302.0 and 303.5 K (Fig. 2a). Their SST distribution is statistically different from that of either the S or the M size category (Table 2).

While the ranges of the TOA albedo distributions are identical among the three size categories, the albedo distributions are slightly positively skewed for the S size category but slightly negatively skewed for the M and L size categories (Fig. 2c). The modes of the distributions also differ by 0.1 between the S and L size categories. This difference is significant when compared to the range of the distributions, which has a value of 0.45 for this type of cloud object. Statistical

significance tests also indicate that the three distributions of TOA albedos are different from each other (Table 2).

The upper limits of outgoing longwave radiation (OLR) fluxes are nearly identical (~175 W m^{-2}) for the three size categories (Fig. 2b) because of the thresholds used in identifying cloud object, i.e., cloud top heights must be greater than 10 km and τ must be greater than 10. The OLR distributions become more positively skewed as the size of cloud objects increases. This is closely related to the significant increase of cloud heights as the size of cloud objects increases (Fig. 2d). The modes of the cloud height distributions differ by 1.5 km between the S and L size categories. These differences are also reflected by those in the cloud top temperature (Fig. 2e), whose modes of the distributions between the S and L size categories differ by more than 10 K. These differences in cloud macrophysical properties are all consistent with the differences shown in OLRs. Each of these three parameters is statistically different among the three size categories (Table 2).

There are two modes in the OLR distributions with values of 124 W m^{-2} and 140 W m^{-2}, in particular, for the S and M size categories (Fig. 2b). There are three closely related interpretations for this feature. First, the abundance of thick anvil clouds in larger size categories may be associated with the 124 W m^{-2} mode while the presence of weak convective updrafts or relatively thin anvils in the smaller size categories may be responsible for the 140 W m^{-2} mode. This bimodal feature is also present in the other periods of analyzed data (Xu et al. 2005), but is most pronounced in the smaller-size categories. Second, the truncation of large, strong convective systems that are located at the edge of the narrow satellite swaths allows the coexistence of both the strong and the weak convective systems in the S and M size categories of cloud objects. Third, the bimodality in the OLR distributions can be associated with the diurnal variation of the tropical deep convection (e.g., Gray and Jacobson 1977; Xu and Randall 1995) because the TRMM precessing orbits allow the sampling of this diurnal variation. A supporting piece of evidence for this interpretation is the lack of this bimodal feature for any of the three size categories in the OLR distribution from the sun-synchronously orbiting Terra satellite during March 2000 (not shown).

The differences in cloud microphysical and optical properties among the three size catego-ries appear to be smaller than those of cloud macrophysical and radiative properties (Figs. 2f-h). In particular, ice particle sizes do not show any statistically significant differences between the S and M size categories or between the S and L size categories according to the bootstrap tests (Table 2). For all three size categories, the distributions of ice water path (IWP) and τ are lognor-mal and exponential in character, respectively (Figs. 2f, h), but there are differences with respect to how sharply the different curves fall from their maxima at the lowest few bins in τ distribu-tions and from the peak at 350 g km^{-2} in IWP distributions. For the smaller-size categories, the probability densities in the higher values of IWP (> 650 g m^{-2}) and τ (> 25) are only slightly dif-ferent. These differences in both IWP and τ may suggest that cumulonimbi and thick anvil clouds are more abundant in the larger-size categories. They also suggest that relatively thin anvils or weak updrafts occur more frequently within the S size cloud objects. These are important results. Further discussion of these results is warranted.

There are several physical explanations why the statistical properties of cloud objects can be different among the three size categories of cloud objects. First, the larger cloud objects are associated with stronger convective systems so that both cumulonimbi and thick anvils penetrate much closer to the tropopause. These characteristics favor large values of IWP, τ, cloud top height and smaller OLR and higher TOA albedo, etc. Second, weaker convective systems or large loosely-organized cloud clusters can be easily broken into several small cloud objects because of the requirement of the contiguous patch of footprints that satisfy the selection criteria. Thus, it is likely that these weaker systems/clusters are a major contributor to the S or M size cloud objects. Their characteristics are more frequently associated with small values of IWP, τ, cloud top height, TOA albedo and large values of OLR, etc. Third, the smaller cloud objects may result from truncation of large cloud systems by the narrow swaths of satellites because some cloud sys-tems are located near the edges of the swaths. If all S size cloud objects result from this trunca-tion, the statistical properties are expected to be similar to those of the L size cloud objects. This is

certainly not the case according to the results shown in Fig. 2. However, there are lower probability densities of the extreme (high or low, depending upon parameters) values in the distributions of the S size category that are comparable to those in the L size category, suggesting that some of the large convective cloud systems are indeed truncated by satellite swaths. This point will become clearer in Section 4 when all three size categories are further classified according to SST ranges.

3c. Linkage with large-scale dynamics

Figs. 3a-c show the frequency diagrams of ω as a function of pressure for the L, M and S size categories, respectively. The bin size for generating the ω frequency is 20 hPa day^{-1}. The layer thickness is 30 hPa. The number of ECMWF grid cells used in calculating the ω frequencies is 13721, 32419 and 53069 for the S, M and L size categories, respectively. It was assumed in the previous section that stronger convective systems can be associated with larger-size cloud objects. This is confirmed by Fig. 3. The vertical velocity frequency for the L size category is higher for large magnitudes of negative ω and lower for the ω range between -150 and + 100 hPa day^{-1} than those of the S and M size categories. Similarities among the three size categories appearing in Figs. 3a-c are 1) the level at which the frequencies have the greatest range of ω is around 600 hPa, which corresponds to the level of the maximum upward motion, and 2) there is a smaller spread above 300 hPa than below 900 hPa.

The differences in the frequency distributions among the three size categories can be more easily seen from the frequencies of ω_{500} (Fig. 3d). Figure 3d shows both the larger negative skewness of the distributions and the shifting of the modes of the distributions towards more negative ω_{500} for larger-size category of cloud objects. The differences at nearly all vertical levels among the three size categories occurs mainly on the upward motion and weak subsidence side of the frequency diagrams (Figs. 3a-c). Although the frequency distributions below 900 hPa and above 450 hPa are concentrated between -100 hPa day^{-1} and +50 hPa day^{-1}, it is easy to notice

that the larger negative skewness of the distributions is found in the larger-size category. The large upward motion below 900 hPa favors intense convection while the strong upward motion above 450 hPa increase the depth and thickness of anvil clouds. Both factors are consistent with the statistical results shown in Fig. 2.

4. Variations of cloud object characteristics with SST

4a. Frequency of occurrence

Table 3 shows the number of cloud objects according to five SST ranges for the three size categories during January-August 1998. The mean SST associated with each cloud object is used to determine which SST range a cloud object belongs to. Each SST range covers an interval of 0.5 K with its midpoint value given in the table, except for the first and last ranges. For the first range (labeled 301.25 K), all cloud objects with mean SSTs between 293.5 K and 301.5 K are included, while all cloud objects with mean SSTs between 303 K and 306 K are included for the last range (labeled 303.25 K).

A few characteristics of the frequency of occurrences are apparent in Table 3. First, there are considerably large numbers of the S and M size cloud objects in the 301.25 K range, i.e., about twice as many as those in the 303.25 K range. Second, more than half of the L size cloud objects occurred in SSTs between 302 and 303 K (263 out of 500). Third, the number of the L size cloud objects in the 303.25 K range is only slightly less than that of 301.25 K range that covers very large SST variations from 293.5 - 301.5 K. These results, in particular, the ratios of L size to all sizes shown in Table 3, indicate that higher SSTs are preferred by the L size cloud objects during the 1998 El Niño period, which is consistent with the result shown by Lin et al. (2005) for the tropical cloud clusters with less stringent selection criteria than those used in the present study.

4b. Statistical properties of cloud objects

Fig. 4 shows a comparison of summary histograms for the L size cloud objects among the five SST ranges. Clearly, the SST histograms are different among these SST ranges. Four of them have narrow distributions with SST variations being less than 2 K, while the 301.25 K range has a

distribution of SST from 293 to 303 K. The high SST end of the distribution is composed of some cloud objects that are narrow and longitudinally oriented and some that are partially located over land, while the low SST end of the distribution is mostly due to other cloud objects with mean SSTs far less than 301 K.

Despite the large differences in the SST distributions, several parameters are similar from one SST range to another, including TOA albedo, IWP, τ and ice particle size (Figs. 4c, f-h). This is confirmed by the statistical significance testing results shown in Table 4, which show the results between the consecutive SST ranges (columns 1-4), the second and fourth SST ranges (column 5) and the first and last SST ranges (column 6). A possible explanation for these observed features is that the L size cloud objects are so optically thick (Fig. 2h) that their optical properties are not impacted by the underlying SSTs. Because of the insensitivity of τ to SST, other retrieved cloud microphysical properties and TOA albedo are also similar among the five SST ranges. Since the S and M size cloud objects have smaller τ, the insensitivity does not hold well, as shown later.

Cloud macrophysical properties such as OLR, cloud height and temperature are rather different among the analyzed SST ranges, except for those between the 301.75 K and 302.25 K ranges (Table 4). For the lower SST ranges, OLR and cloud temperature tend to be more negatively skewed while cloud height tends to be more positively skewed. The differences in the modes of the distributions of cloud height and temperature between the 301.25 K and 303.25 K ranges are as great as or greater than those between the S and L size categories of cloud objects discussed earlier (Fig. 2). In OLR, the mode at 140 W m^{-2} is more pronounced for the lower SST ranges. This result can, as shown later, be related to weaker large-scale ascents of cloud objects in the lower SST ranges, resulting in relatively shallower convective systems.

Besides the differences discussed in Section 3b, the M size category has slightly different and sometimes stronger dependency of their properties on the SST ranges (Figs. 5a, c, e, g), compared to the L size category. First, cloud microphysical and optical properties show slightly more significant differences among some of the SST ranges (Table 5). For example, the cloud objects in

the 301.25 K range are more reflective (higher albedo) than those in the other four SST ranges (Fig. 5a). The probability densities at the lowest bin of τ show larger spreads among the different SST ranges (not shown), relative to the L size category (Fig. 4h). Second, similar distributions of cloud macrophysical properties and OLR are found between the 302.25 K and 302.75 K ranges, instead of between the 301.75 K and 302.25 K ranges as found in the L size category. A larger SST bin width for classifying cloud objects would probably not reveal this difference between these two size categories.

The S size category of cloud objects shows more similarities with the large-size category of cloud objects (Figs. 5b, d, f, h and Table 6) in terms of how the cloud properties change with SSTs, especially in cloud microphysical and optical properties, compared to the M size category. First, TOA albedo and τ show small differences among the analyzed SST ranges (Table 6) although the distributions of ice particle sizes show significant difference among some SST ranges. Second, cloud macrophysical properties are rather similar among the three highest SST ranges (Table 6). Their distributions for the two lowest SST ranges are, however, different from those of the three highest SST ranges and are also different from each other. The distributions of the lowest SST ranges have pronounced peaks in OLR between 140 and 150 W m^{-2} while the peak at 124 W m^{-2} basically disappears. The latter peak is associated with strong convective systems. These results suggest that many of the S size cloud objects in the three highest SST ranges may be associated with strong convective systems that are split by satellite swaths and/or strong/ growing convective systems that had not yet reached the L size category, as far as their macrophysical properties are concerned (compare Figs. 5d, f, h with Figs. 2b, d, e).

4c. Linkage with large-scale dynamics

The ω frequency departures from Fig. 3a are plotted in Fig. 6 for all five SST ranges of the L size category. The magnitude of the departures exceeding 0.6% appears very often, with some exceeding 1.0%, which is the lowest shaded value plotted in Fig. 3a. Two distinct features can be pointed out from Fig. 6. First, higher frequent occurrences of upward motion ($\omega < $ -50 hPa

day^{-1}) are seen in the lowest 150 hPa in the lowest SST ranges while the opposite is true for the highest SST ranges. This means that stronger low-level upward motion, which acts as a trigger, is required to produce large convective systems when the SST is lower. Second, the differences in cloud macrophysical properties shown in Fig. 4 cannot be explained by those in the vertical velocity frequency alone. For example, the 301.75 K and 302.25 K ranges show no significant difference in cloud macrophysical properties, but there are more frequent occurrences of upward motions in the 301.75 K range. Therefore, the higher SST in the 302.25 K range has to compensate for the weaker ascent motions. Another example to support this point is the overall similarity in ω frequency distributions (i.e., small departures) between the 302.25 K and 302.75 K ranges, but the cloud macrophysical properties are different between these two SST ranges (Table 4).

The frequency distributions of ω_{500} for the five SST ranges are shown in Fig. 7 for all three size categories. First, the differences in the ω_{500} distribution are greater between some pairs of SST ranges for the S and M size categories, compared to the L size category. This is also true for other heights, especially in the lower troposphere. For example, the frequencies corresponding to the modes of the 301.25 K and 303.25 K distributions differ by ~2% both the S and M size categories. Second, the large differences among pairs of SST ranges occur mainly over the negative ω_{500} side of the diagrams, suggesting that the SST differences can impact the ascent regions of the matched cloud object regions, i.e., cloud objects themselves. All of these results suggest that impact of SST on the large-scale dynamics seems to be stronger for the smaller-size categories of cloud objects. The combination of SST with large-scale dynamics may explain the larger differences in the statistical properties between some pairs of the five SST ranges shown in Fig. 5.

5. Variations of cloud object characteristics with satellite precessing cycle

5a. Frequency of occurrence

Table 7 shows the number of cloud objects in the Pacific classified according to satellite precessing cycles. The numbers of cloud objects are obtained for five precessing cycles of each of

the three size categories. The precessing cycle of the TRMM satellite is 46 days long. The first precessing cycle was selected to begin from January 14, 1998 (end on 28 February) instead of January 1, 1998 for the sake of labeling these cycles, which is labeled "January-February" ("Jan-Feb" for short) cycle. The other precessing cycles are labeled as Mar-Apr (Mar. 1 - Apr. 15), Apr-May (Aprl 16 - May 31), Jun-Jul (June 1 - July 16), and Jul-Aug (July 17 - Aug. 31), respectively.

It appears that the total number of all-size cloud objects in each precessing cycle is roughly the same, i.e., within 20% of each other (last row in Table 7). The differences in the number of cloud objects among the precessing cycles are larger for individual size categories. The number of cloud objects in the S size category is the largest in the Jul-Aug cycle and the smallest in the Jan-Feb cycle. The M size cloud objects also have the largest number of occurrences in the Jul-Aug cycle. This result is related to low SSTs. The L size category has a higher number of cloud objects in the Jan-Feb cycle, corresponding to the peak phase of the 1997/1998 El Niño.

5b. Statistical properties of cloud objects

Fig. 8a shows the SST distributions of the L size category for five precessing cycles. From January to August 1998, the probability densities for SSTs greater than 302 K decrease as the El Niño dissipates. This is indicated by the shift in distribution towards the lower SSTs with the precessing cycle progressing. The SST distribution is close to be normally distributed in the Jul-Aug cycle. In the other four cycles, the SST pdfs are skewed towards higher SSTs. The statistical significance tests show that the SST distributions between most pairs of the precessing cycles are statistically different (Table 8), especially those of non-consecutive cycles. The exceptions are between the first two precessing cycles during the peak period of the El Niño and between the Apr-May and Jun-Jul cycles.

Visual inspection of the rest of the panels in Fig. 8 shows that the spread of the five precessing-cycle distributions is not as great as that seen from Fig. 4 among the five SST range distributions for cloud macrophysical properties, but slightly greater for cloud microphysical and optical properties and TOA albedo. These are important distinctions between these two sets of

results because differences in the collective large-scale dynamics (for an ensemble of cloud objects) among the precessing cycles tend to be smaller than those among the SST ranges. This is because an ensemble of cloud objects are sampled from the entire tropical Pacific region within a given precessing cycle instead of a few selected subregions within an SST interval. In both sets of categorization, only parts of the ascent branch of the Hadley circulations are included.

The most important parameter for validating the FAT hypothesis of Hartmann and Larson (2002), as discussed in the introduction, is the cloud top temperature. All pdfs of cloud top temperature are nearly normally distributed except for being slightly skewed towards the high values of cloud top temperature (Fig. 8e). The most striking feature shown in Fig. 8e is that most of the pdfs are not statistically different from each other despite the large differences in the SST distributions among some precessing cycles (Table 8). The exceptions are the moderate differences between the Mar-Apr and Apr-May cycles and between the Jan-Feb and Jul-Aug cycles, with p values being between 0.05 and 0.10. These differences among some pairs of precessing cycles appear mainly in the high temperature ranges (>215 K), but not in the low temperature ranges. For the purpose of comparison, this statement is not true for the different SST ranges (Fig. 4e) shown in Section 4b. The similarity in the low temperature ranges of pdfs among the precessing cycles, therefore, suggests that the FAT hypothesis of Hartmann and Larson (2002) is basically valid.

Similarly, the OLR distributions are only moderately different among some precessing cycles, except for between the first and last cycles which are statistically different. This is because the OLR flux is proportional to the fourth power of cloud top temperature for thick anvil clouds. A small difference in cloud top temperature thus results in a significant difference in OLR.

Cloud height is another cloud macrophysical property that shows no statistically significant differences among the precessing cycles except for between the first and last precessing cycles (Table 8). This result can be visually confirmed from Fig. 8d. This parameter is obviously related to the strength of large-scale dynamics because stronger large-scale ascent can increase the overall cloud height of convective systems, which can skew the cloud height distribution towards higher values. The lack of the statistically significant differences in cloud height among the pre-

cessing cycles thus further supports the validity of the FAT hypothesis. As discussed in Part I, cloud top height can be different if the stratification of the atmosphere changes significantly, for example, between the Jan-Feb (the peak phase of El Niño) and Jul-Aug (the dissipative phase of El Niño) cycles.

The statistically significant differences in cloud microphysical properties, TOA albedo and τ among some precessing cycles for the L size category are related to the distributions in one or two particular precessing cycles that are very different from other precessing cycles (Fig. 9 and Table 8). They are the Mar-Apr cycle in τ and TOA albedo, the Jun-Jul cycle in IWP, and Mar-Apr and Jun-Jul cycles in ice particle size, in addition to significant or moderately significant differences between the first and last precessing cycles in IWP, ice particle size and τ.

For the S and M size cloud objects, the differences in SST distribution between two precessing cycles are not necessarily larger than those of the L size cloud objects (Tables 8 - 10). The last two precessing cycles show significant differences in the SST distributions from the earlier cycles and between each other. However, these differences do not translate into statistically significant differences in cloud macrophysical and microphysical properties. As in cloud microphysical and optical properties of the L size category, one or two particular precessing cycles show the most pronounced differences from the other precessing cycles. For cloud height, temperature and OLR, significantly different cycles are found for the Mar-Apr of the M size category and the Jun-Jul of the S size category (Fig. 9). Most of the cloud microphysical properties and TOA albedo, however, are not significantly different from other precessing cycles for these particular precessing cycles. This result is similar to that found in the different SST ranges discussed in Section 4b. This similarity suggests that the collective large-scale dynamics may be less similar among precessing cycles for the S and M size categories, compared to that of L size category, implying that the FAT hypothesis is probably less valid for the S and M size categories.

5c. Linkage with large-scale dynamics

The ω frequency departures from Fig. 3a are plotted in Fig. 10 for all five precessing cycles of the L size category. The magnitudes of the departures are mostly between -0.2% and +0.2%, with small areas over 1.0%. The small differences in both the large-scale dynamics and SST among the precessing cycle contribute to small differences in cloud macrophysical properties, compared to those among the SST ranges discussed in Section 3b. This does not mean that there are no differences in the ω frequency diagrams among the five precessing cycles. For example, the frequency distributions of the Jul-Aug cycle (low SST) at all heights are more skewed toward higher magnitudes of upward motion, compared to those of the Jan-Feb cycle (high SST). The stronger vertical motions, thus, compensate for the lower SSTs for the Jul-Aug cycle.

The differences among the five precessing cycles are generally larger for the S and M size categories than for the L size category. This can be seen from the frequency distributions of ω_{500} for the five precessing cycles (Fig. 11) of all three size categories. For example, the frequency difference corresponding to the modes of ω_{500} between the Jan-Feb and Jul-Aug cycles of the S size category is about 3%. It is about half as large for the M size category, but less than 0.5% for the L size category. This result suggests that large-scale dynamics are more likely to be different for the smaller size categories of cloud objects. Consequently, the differences in cloud macrophysical properties are larger for the S and M size cloud objects among some precessing cycles, compared to the L size cloud objects (Fig. 9).

6. Conclusions and discussion

In this study, characteristics of tropical convective cloud objects observed over the tropical Pacific during January-August 1998 have been examined using the TRMM/CERES SSF data, with an emphasis on validating the fixed anvil temperature (FAT) hypothesis of Hartmann and Larson (2002). These characteristics include the frequencies of occurrence and statistical distributions of cloud microphysical, macrophysical, optical and radiative properties. Their variations

with cloud object size, SST and satellite precessing cycle have been analyzed, as well as the cor-responding distributions of the matched vertical velocity.

It is found that statistical distributions of cloud physical properties are significantly differ-ent among three size categories of cloud objects with equivalent diameters of 100 - 150 km, 150 - 300 km, and > 300 km, respectively, except for those of ice particle size. The distributions for the larger-size category of cloud objects are more skewed towards high SSTs, high cloud tops, low cloud-top temperature, large ice water path, high τ, low outgoing LW radiation, and high TOA albedo than the smaller-size category. Physical interpretations for these differences are that the larger cloud objects are associated with stronger convective systems so that both cumulonimbi and thick anvils penetrate closer to the tropopause. The weaker convective systems or loosely organized cloud clusters, on the other hand, can be easily broken into several small cloud objects because of the contiguous requirement of the cloud object definition. Very few small-size cloud objects result from truncation by narrow satellite swaths from the strong convective systems. The frequency distributions of the matched ω confirm that there are significant differences in the large-scale dynamics among the three size categories of cloud objects. These distributions of ω are more negatively skewed for larger-size cloud objects that favor the existence of stronger con-vective systems.

As SST varied from one satellite precessing cycle to another, the changes in macrophysi-cal properties of cloud objects over the entire tropical Pacific were small for the large-size cate-gory of cloud objects, relative to those of the small- and medium-size categories. This result suggests that the FAT hypothesis may be valid for the large-size category. Combining with the result that a higher percentage of the large-size category of cloud objects occurs during higher SST subperiods, this implies that macrophysical properties of cloud objects would be less sensi-tive to further warming of the climate if the collective large-scale dynamics remain relatively unchanged. It is also found that some cloud microphysical properties, TOA albedo and τ, are sig-nificantly different between some precessing cycles for the large size category even though cloud macrophysical properties are not. This characteristic is found in the small- and medium-size cloud

objects for some pairs of precessing cycles. The frequency distributions of the matched large-scale vertical velocity show small differences among the precessing cycles for the large-size category, relative to those for the small- and medium-size categories. This is consistent with the observation that statistical distributions of cloud macrophysical properties are not significantly different among the precessing cycles for the large-size category.

On the other hand, the large-scale dynamics play more important roles in the cloud objects when they are classified as a function of SST instead of as a function of satellite precessing cycles. Statistical characteristics of cloud microphysical properties, optical depth and TOA albedo are not sensitive to the SST, but those of cloud macrophysical properties including cloud top temperature are strongly dependent upon the SST. This feature is also present in some of the five precessing cycles of the small- and medium-size categories of cloud objects. This is due to the fact that large-scale dynamics are less similar for these precessing cycles of the small- and medium-size categories of cloud objects.

Further studies will be performed to compare statistical properties from observations and high-resolution cloud model simulations to firmly validate the FAT hypothesis. Preliminary results from one-month simulation of tropical convective cloud objects show that a 2-D CRM can do a better job in capturing the differences in cloud microphysical properties among three size categories than those for the cloud macrophysical properties. This result may suggest that it might be difficult to validate the FAT hypothesis with 2-D CRM simulations. Further study will be needed to investigate the ability of 3-D CRMs in capturing these observed differences.

References

Cess, R. D., M. Zhang, P.-H. Wang and B. A. Wielicki, 2001: Cloud structure anomalies over the tropical Pacific during the 1997/98 El Niño. *Geophys. Res. Lett.*, **28**, 4547-4550.

Efron, B. and R. Tibshirani, 1993: *An Introduction to the Bootstrap.* Chapman & Hall, New York, 456 pp.

Eitzen, Z. A. and K.-M. Xu, 2005: A statistical comparison of deep convective cloud objects observed by an Earth Observing System satellite and simulated by a cloud-resolving model. *J. Geophys. Res.,* **110,** D15S14, doi: 10.1029/2004JD005086.

Fu, Q., M. Baker, and D. L. Hartmann, 2002: Tropical cirrus and water vapor: An effective Earth infrared iris?. *Atmos. Phy. Chem.,* **2,** 31-37.

Gray, W. M., and R. W. Jacobson, Jr., 1977: Diurnal variation of deep cumulus convection. *Mon. Wea. Rev.,* **105,** 1171-1188.

Hartmann, D. L., and K. Larson, 2002: An important constraint on tropical cloud-climate feed-back. *Geophys. Res. Lett.,* **29,** No. 20, 1951, doi:10.1029/2002GL015835.

Hartmann, D.L., and M.L. Michelsen, 1993: Large-scale effects on regulation of tropical sea surface temperature. *J. Climate,* **6,** 2049-2062.

Hartmann, D. L., and M. L. Michelsen, 2002: No evidence for iris. *Bull. Amer. Meteor. Soc.,* **83,** 249-254

IPCC, 2001: Intergovernmental Panel on Climate Change, *Climate Change 2001,* Third Assessment Report of the IPCC. The Scientific Basis. A contribution of Working Group I. Cambridge University Press.

Khairoutdinov, M. F., and D. A. Randall, 2001: A cloud-resolving model as a cloud parameterization in the NCAR Community Climate System Model: Preliminary results. *Geophys. Res. Lett.* **28,** 3617-3620.

Larson, K., and D. L. Hartmann, 2003a: Interactions among cloud, water vapor, radiation, and large-scale circulation in the tropical climate. Part I: Sensitivity to uniform sea surface temperature changes. *J. Climate,* **16,** 1425-1440.

Larson, K., and D. L. Hartmann, 2003b: Interactions among cloud, water vapor, radiation, and large-scale circulation in the tropical climate. Part II: Sensitivity to spatial gradients of sea surface temperature. *J. Climat*e, **16,** 1441-1455.

Lau, K.-M., C.-H. Sui, M.-D. Chou and W.-K. Tao, 1994: Cirrus cloud thermostat effect for tropical sea surface temperature-fact or fiction. *Geophy. Res. Lett.,* **21,** 1157-1160.

Lin, B., B. A. Wielicki, L. H. Chambers, Y. Hu, and K.-M. Xu, 2002: The iris hypothesis: A negative or positive cloud feedback?. *J. Climate*, **15,** 3–7.

Lin, B., B. A. Wielicki, P. Minnis, L. H. Chamber, K.-M. Xu, Y. Hu, and A. Fan, 2005: The effect of environmental conditions on tropical deep convective systems observed from the TRMM satellite. *J. Climate,* (conditionally accepted).

Lindzen, R., M.-D. Chou, and A. Hou, 2001: Does the earth have an adaptive infrared iris?. *Bull. Amer. Meteor. Soc.,* **82**, 417–432.

Loeb, N. G., N. Manalo-Smith, S. Kato, W. F. Miller, S. K. Gupta, P. Minnis, and B. A. Wielicki, 2003: Angular distribution models for top-of-atmosphere radiative flux estimation from the Clouds and the Earth's Radiant Energy System instrument on the Tropical Rainfall Measuring Mission satellite. Part I: Methodology. *J. of Appl. Meteor.*, **42,** 240–265.

Minnis, P.; D. Y. Young, D. P. Kratz; J. A. Coakley, Jr.; M. D. King, D. P. Garber, P. W. Heck, S. Mayor, and R. F. Arduini, 1997: Cloud Optical Property Retrieval (Subsystem 4.3). "Clouds and the Earth's Radiant Energy System (CERES) Algorithm Theoretical Basis Document, Volume III: Cloud Analyses and Radiance Inversions (Subsystem 4)," edited by CERES Science Team, December, 1997, 60 pp. [http://asd-www.larc.nasa.gov/ATBD/ATBD.html]

Ohring, G., B. A. Wielicki, R. Spencer, B. Emery and R. Datla, 2005: Satellite instrument calibration for measuring global climate change. Report of a workshop. *Bull. Amer. Meteor. Soc.,* **86,** 1303-1313, doi: 10.1175/BAMS-86-9-1303.

Ramanathan, V. and W. Collins, 1991: Thermodynamic regulation of ocean warming by cirrus clouds deduced from observations of the 1987 El Niño. *Nature*, **351**, 27-32.

Randall, D. A., M. Khairoutdinov, A. Arakawa, and W. Grabowski, 2003: Breaking the cloud parameterization deadlock. *Bull. Amer. Meteor. Soc., * **84,** 1547-1564.

Wielicki, B. A., and R. M. Welch, 1986: Cumulus cloud properties derived using Landsat satellite data. *J. Clim. Appl. Meteor.,* **25,** 261-276.

Wielicki, B. A., R. D. Cess, M. D. King, D. A. Randall, and E. F. Harrison, 1995: Mission to Planet Earth: Role of clouds and radiation in climate. *Bull. Amer. Meteor. Soc.,* **76,** 2125-2153.

Wielicki, B. A., B. R. Barkstrom, E. F. Harrison, R. B. Lee III, G. L. Smith, and J. E. Cooper, 1996: Clouds and the Earth's Radiant Energy System (CERES): An Earth Observing System Experiment. *Bull. Amer. Meteor. Soc.*, 77, 853-868.

Xu, K.-M., 2005: Applying the bootstrap method for statistical significance test of differences between histograms. *Mon. Wea. Rev.* (in press).

Xu, K.-M., and D. A. Randall, 1995: Impact of interactive radiative transfer on the macroscopic behavior of cumulus ensembles. Part II: Mechanisms for cloud-radiation interactions. *J. Atmos. Sci.*, **52**, 800- 817.

Xu, K.-M., and D. A. Randall, 1996: Explicit simulation of cumulus ensembles with the GATE Phase III data. Comparison with observations. *J. Atmos. Sci.*, **53**, 3710-3736.

Xu, K.-M., and D. A. Randall, 2000: Explicit simulation of cumulus ensembles in midlatitude: Comparison with ARM observations. *J. Atmos. Sci.,* **57**, 2839-2858.

Xu, K.-M., T. Wong, B. A. Wielicki, L. Parker, and Z. A. Eitzen, 2005: Statistical analyses of satellite cloud object data from CERES. Part I: Methodology and preliminary results of 1998 El Niño/2000 La Niña. *J. Climate,* **18,** 2497-2514.

Figure captions

Fig. 1: A schematic of the approach for cloud object observation and modeling to understand cloud feedbacks.

Fig. 2: Summary histograms for (a) sea surface temperature, (b) outgoing longwave radiation, (c) top-of-the-atmosphere albedo, (d) cloud top height, (e) cloud top temperature, (f) ice water path, (g) ice particle size, and (h) cloud optical depth of tropical convective cloud objects for the January-August 1998. Three different size categories of cloud objects are shown.

Fig. 3: Frequency diagrams of vertical velocity as a function of pressure for (a) large-size, (b) medium-size and (c) small-size categories of cloud objects. The bin size is 20 hPa day^{-1}. The values corresponding to different shading areas from the darkest to the white areas near 0 hPa day^{-1} are 0.01, 0.03, 0.05, 0.07, 0.09, 0.13 and 0.15. The frequency diagram of ω_{500} for all three size categories is shown in (d).

Fig. 4: Same as Fig. 2 except for large-size category of cloud objects classified according to different SST ranges.

Fig. 5: Same as Fig. 4 except for the variations of medium- (a, c, e, f) and small-size (b, d, f, h) cloud objects on SST ranges. TOA albedo, OLR, cloud temperature and height are shown.

Fig. 6: The distributions of vertical velocity frequency departures from that of the entire eight-month period (Fig. 3a) for five SST ranges of the large-size category of cloud objects. The red areas indicate positive departures while the blue areas indicate negative departures. From the lightest to darkest shades, the frequency departures range from 0.002, 0.006, 0.010 to 0.020.

Fig. 7: The frequency distribution of ω_{500} for five SST ranges of the (a) large-size, (b) medium-size, and (c) small-size categories of cloud objects.

Fig. 8: Same as Fig. 2 except for the large-size category of cloud objects classified according to satellite precessing cycles.

Fig. 9: Same as Fig. 2 except for four parameters for the small- (b, d, f, and h) and medium-size (a, c, e, and g) categories of cloud objects classified according to satellite precessing cycles.

Fig. 10: Same as Fig. 6 except for the five precessing cycles.

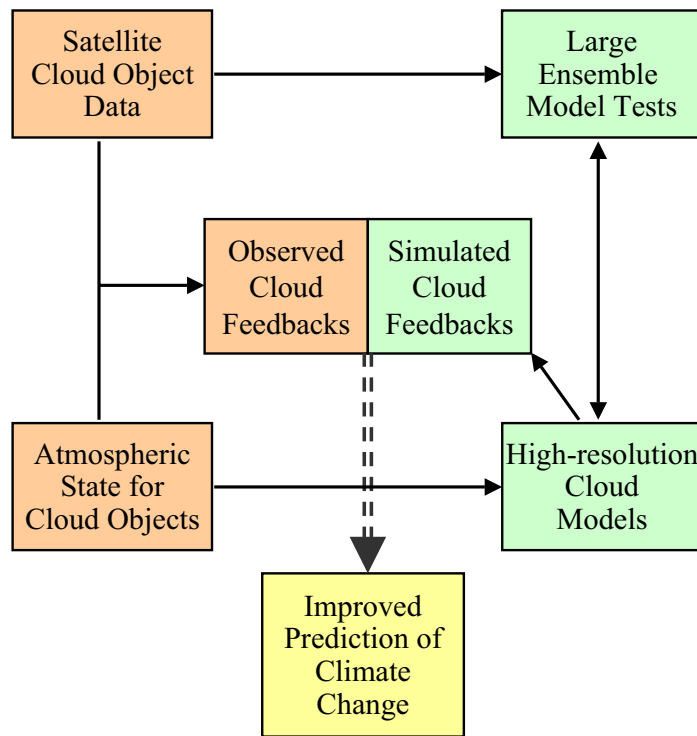Fig. 11: Same as Fig. 7 except for the five precessing cycles.

Figure 1: A schematic of the approach for cloud object observation and modeling to understand cloud feedbacks.
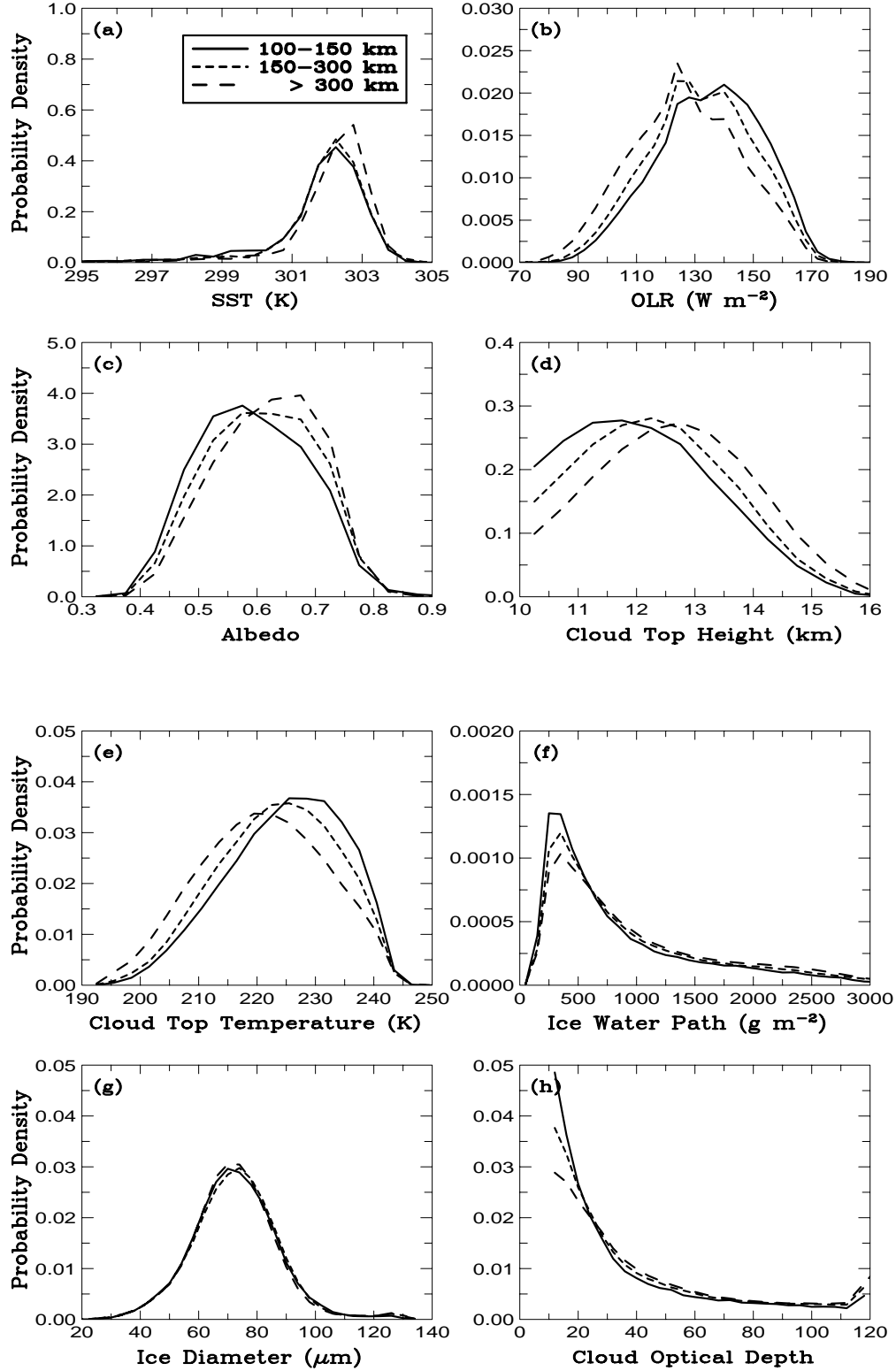
Figure 2: Summary histograms for (a) sea surface temperature, (b) outgoing longwave radiation, (c) top-of-the-atmosphere albedo, (d) cloud top height, (e) cloud top temperature, (f) ice water path, (g) ice particle size, and (h) cloud optical depth of convective cloud objects for the January-August 1998. Three different size categories of cloud objects are shown.
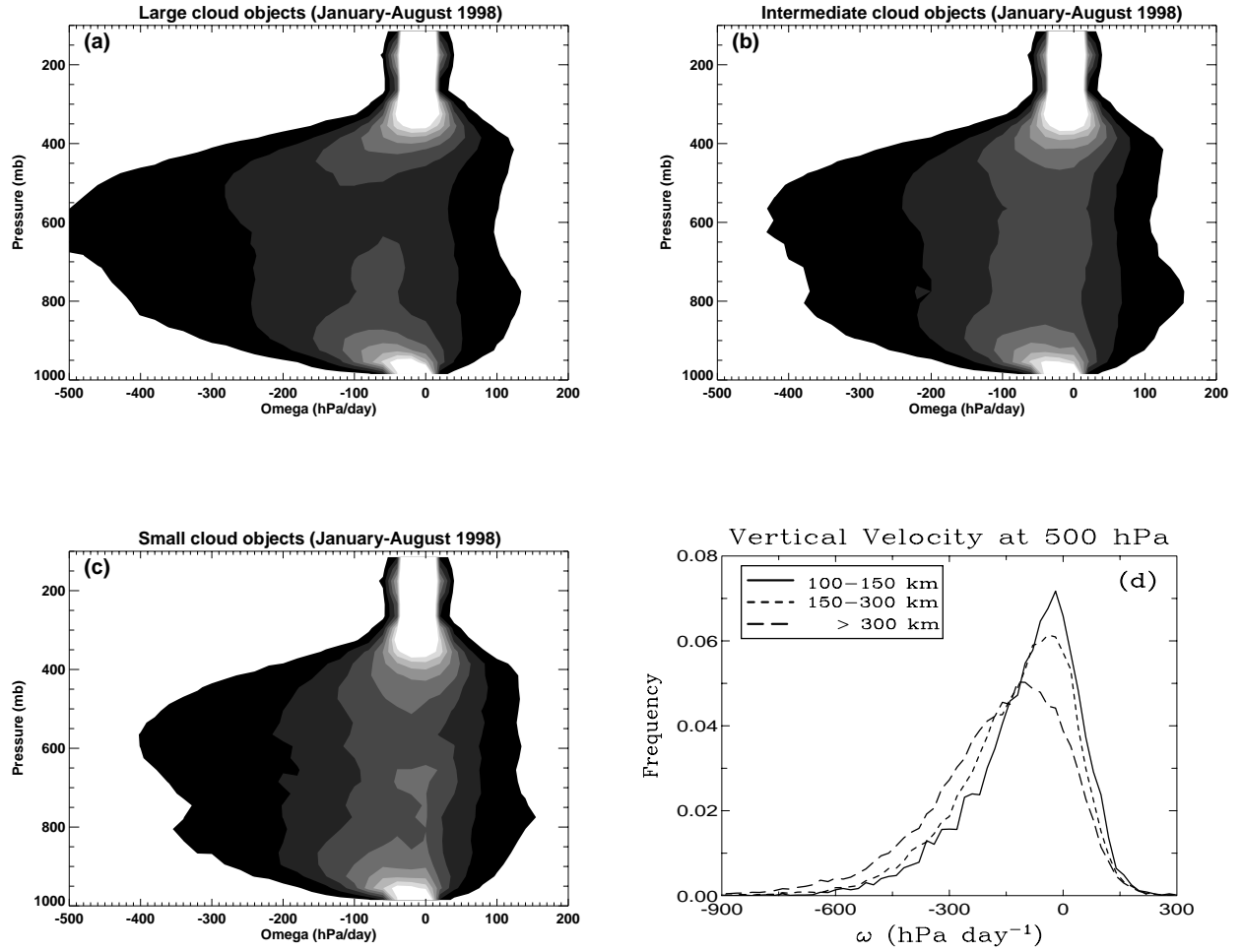
Figure 3: Frequency diagrams of vertical velocity as a function of pressure for (a) large-size, (b) medium-size and (c) small-size categories of cloud objects. The bin size is 20 hPa day^{-1}. The values corresponding to different shading areas from the darkest to the white areas near 0 hPa day^{-1} are 0.01, 0.03, 0.05, 0.07, 0.09, 0.13 and 0.15. The frequency diagram of ω_{500} for all three size categories is shown in (d).
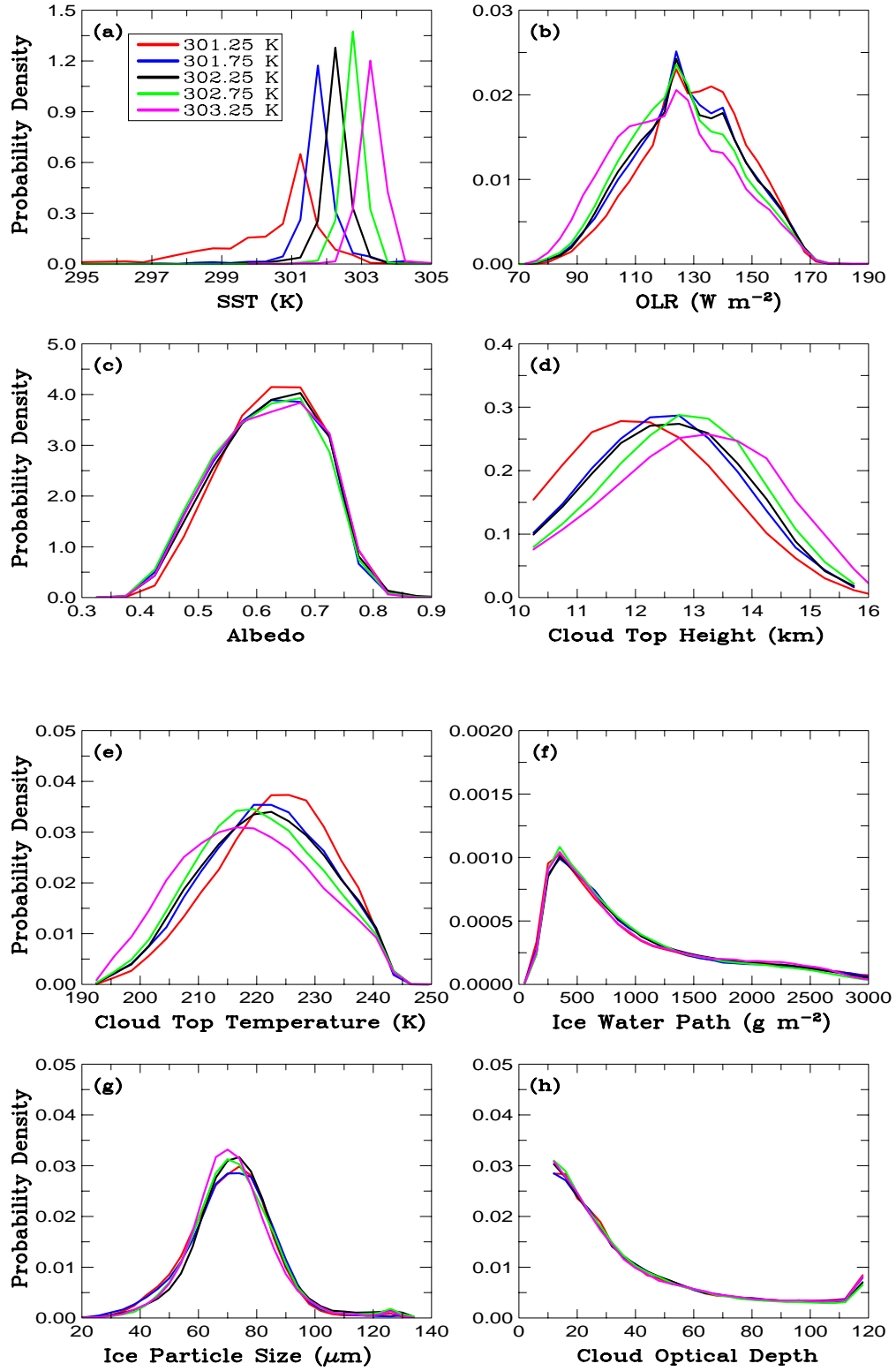
Figure 4: Same as Fig. 2 except for the large-size category of cloud objects classified according to different SST ranges.
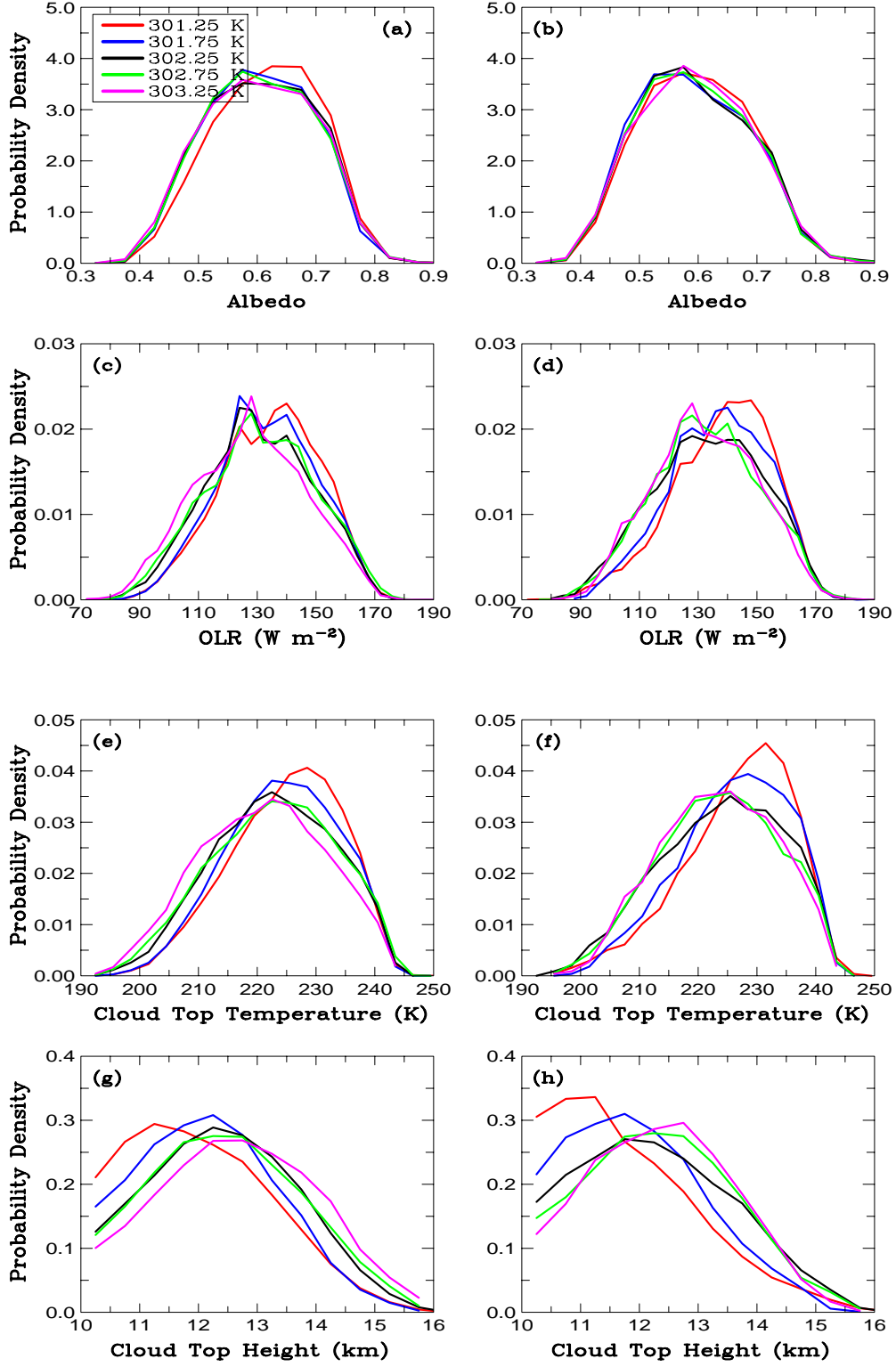
Figure 5: Same as Fig. 4 except for the variations of medium- (a, c, e, f) and small-size (b, d, f, h) cloud objects on SST ranges. TOA albedo, OLR, cloud temperature and height are shown.
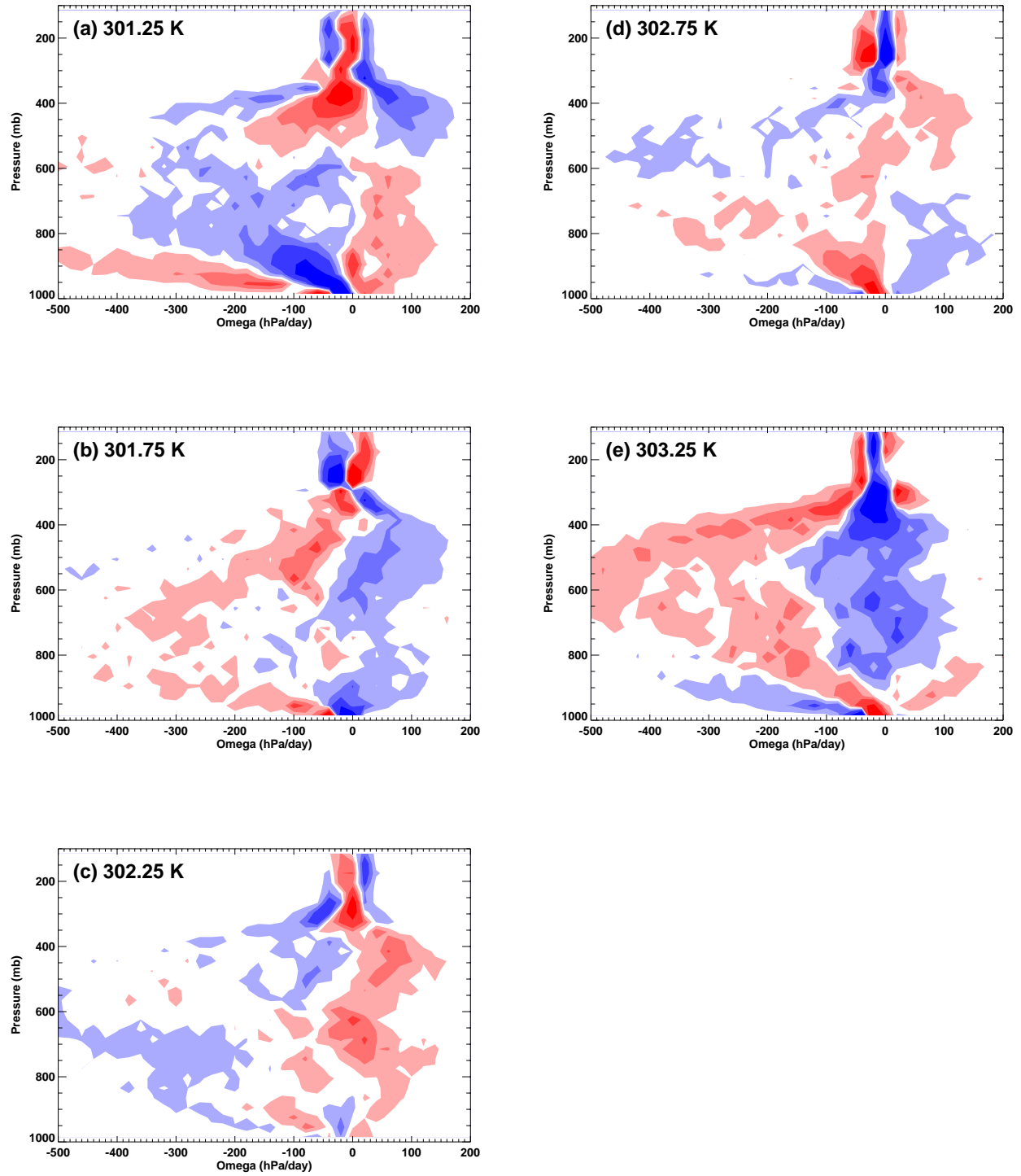
Figure 6: The distributions of vertical velocity frequency departures from that of the entire eight-month period (Fig. 3a) for five SST ranges of the large-size category of cloud objects. The red areas indicate positive departures while the blue areas indicate negative departures. From the lightest to darkest shades, the frequency departures range from 0.002, 0.006, 0.010 to 0.020.
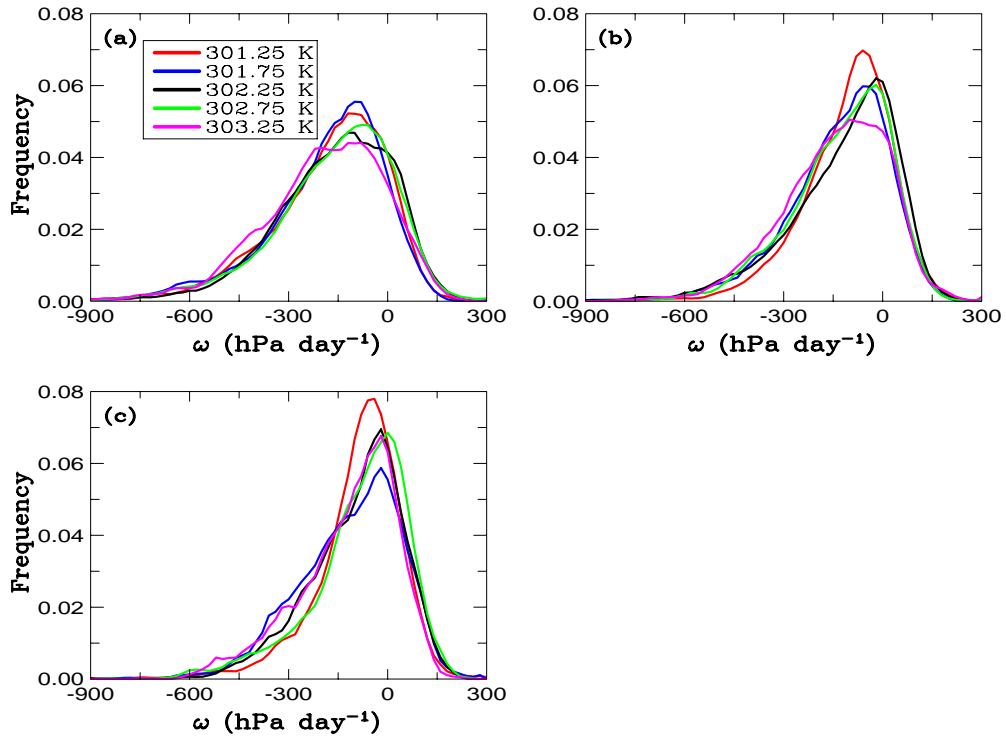
Figure 7: The frequency distribution of ω_{500} for five SST ranges of the (a) large-size, (b) medium-size, and (c) small-size categories of cloud objects.
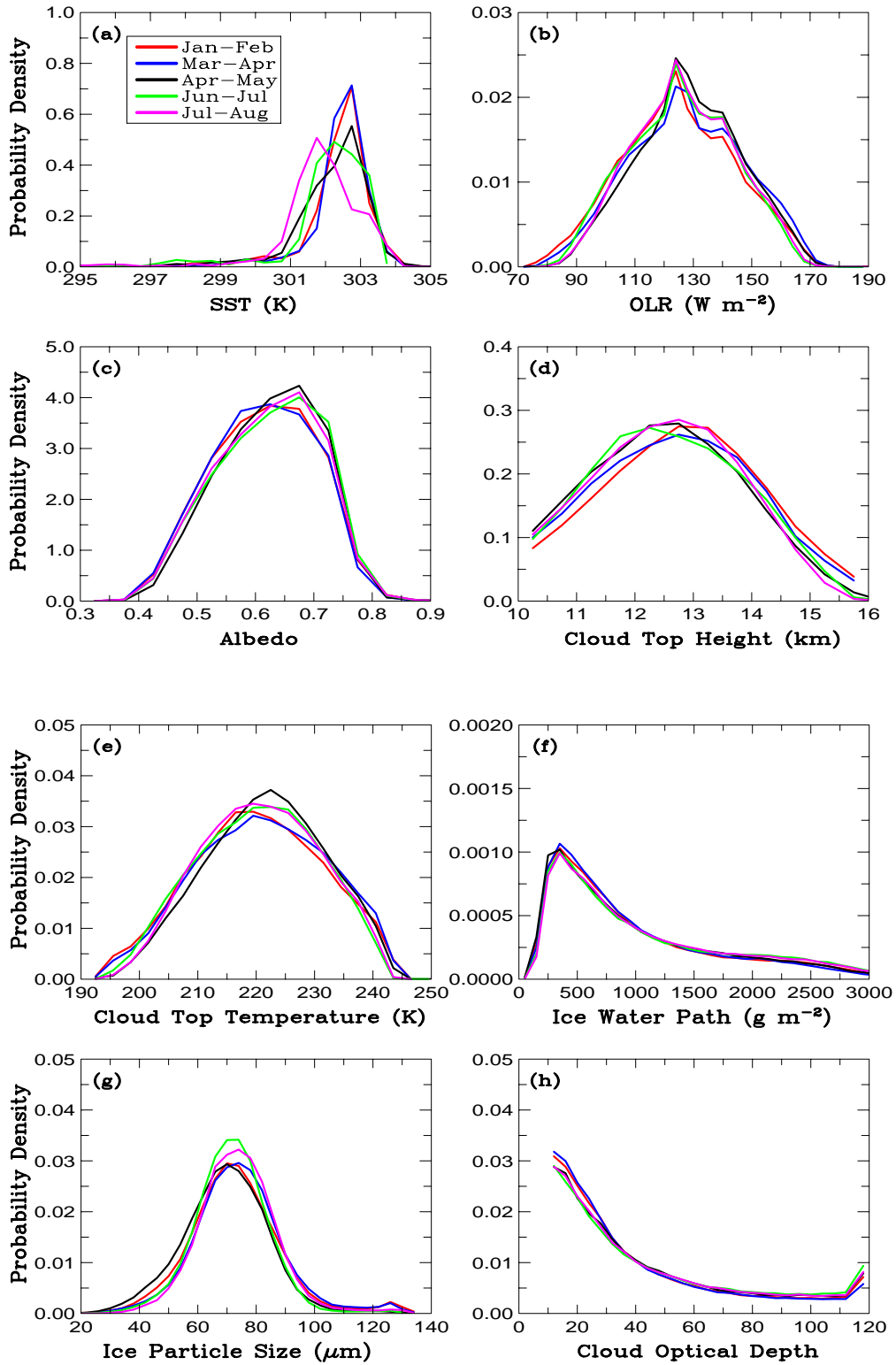
Figure 8: Same as Fig. 2 except for the large-size category of cloud objects classified according to satellite precessing cycles.
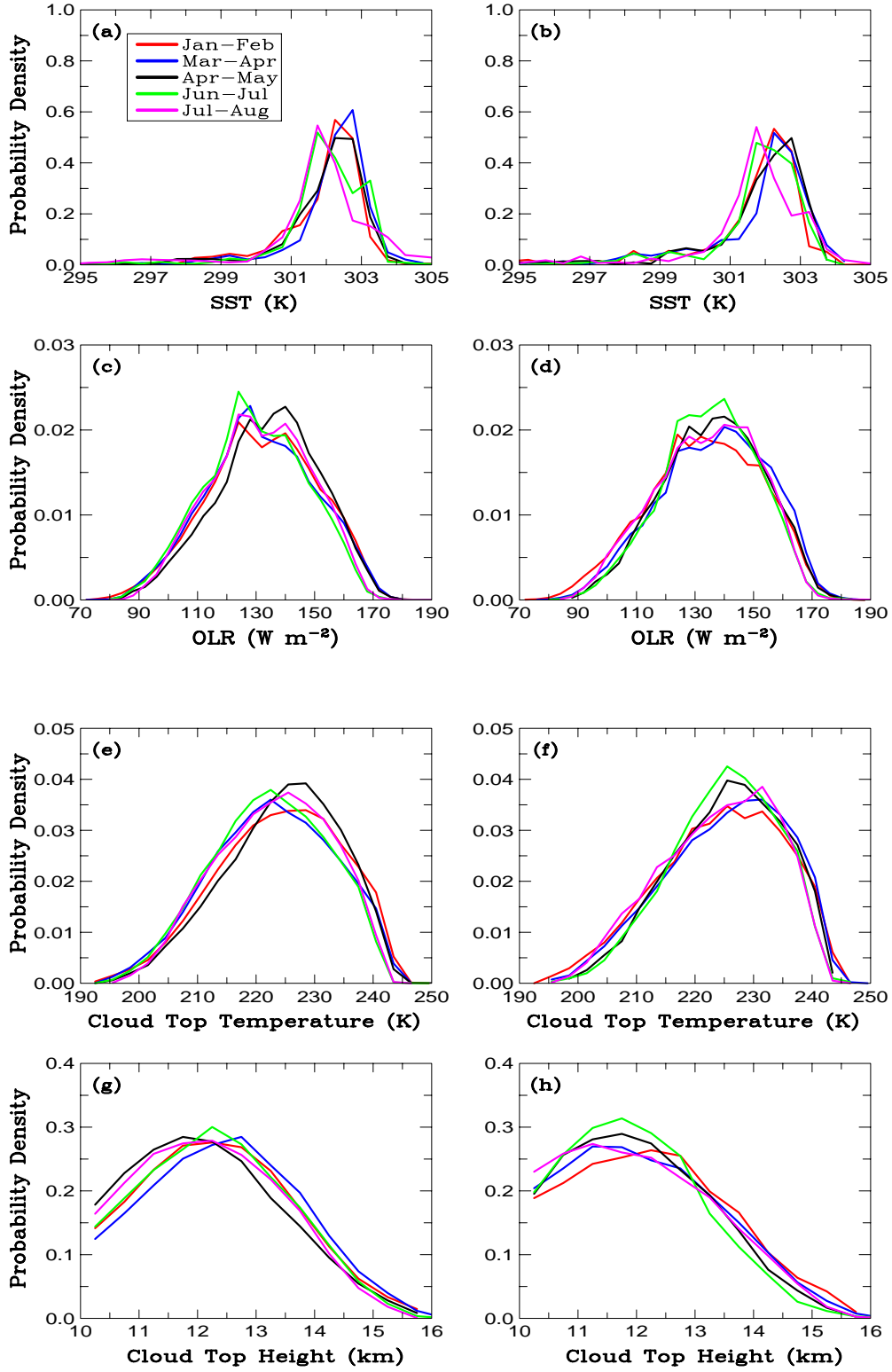
Figure 9: Same as Fig. 2 except for four parameters for the small- (b, d, f, and h) and medium-size (a, c, e, and g) categories of cloud objects classified according to satellite precessing cycles.
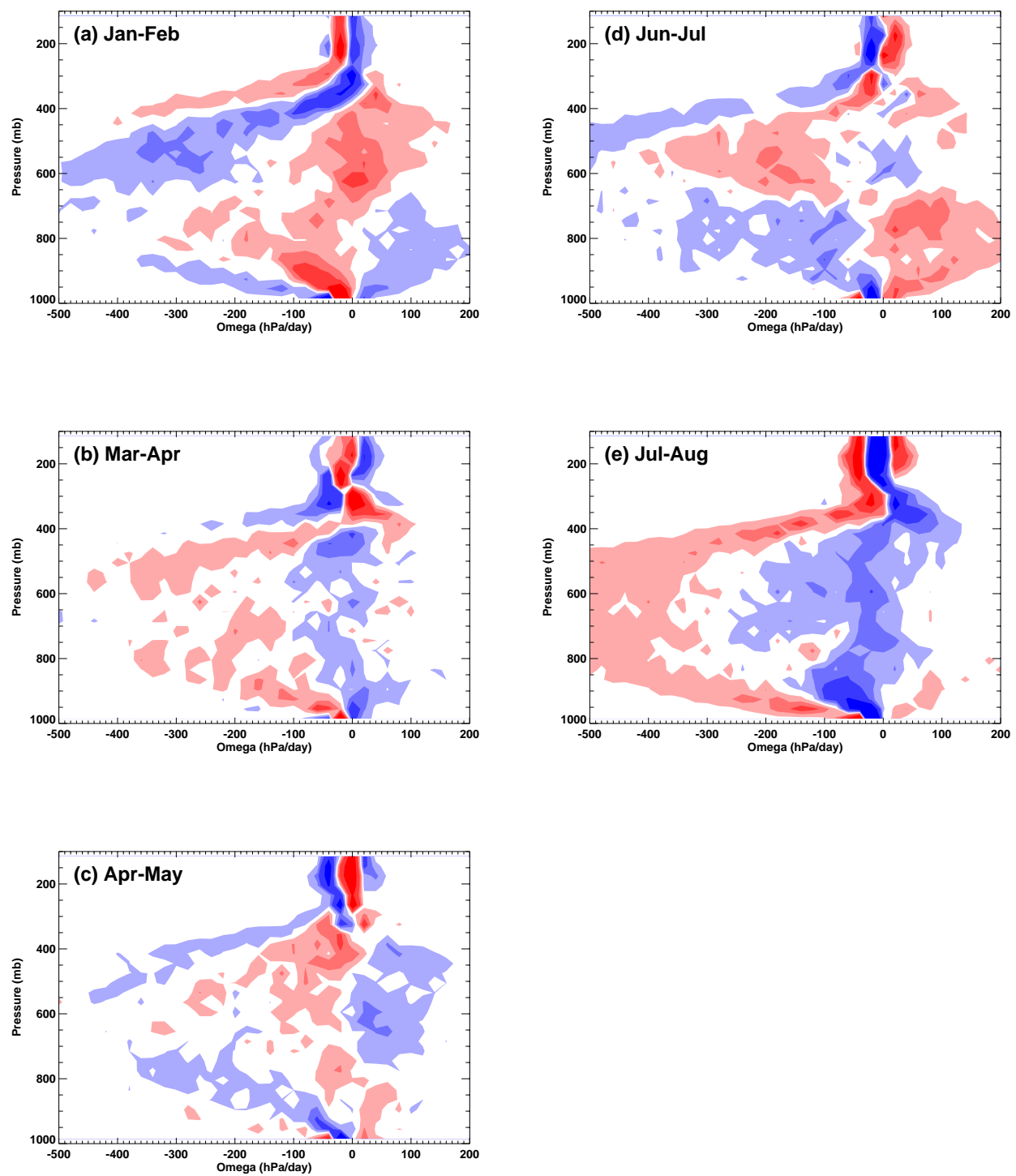
Figure 10: Same as Fig. 6 except for the five precessing cycles.
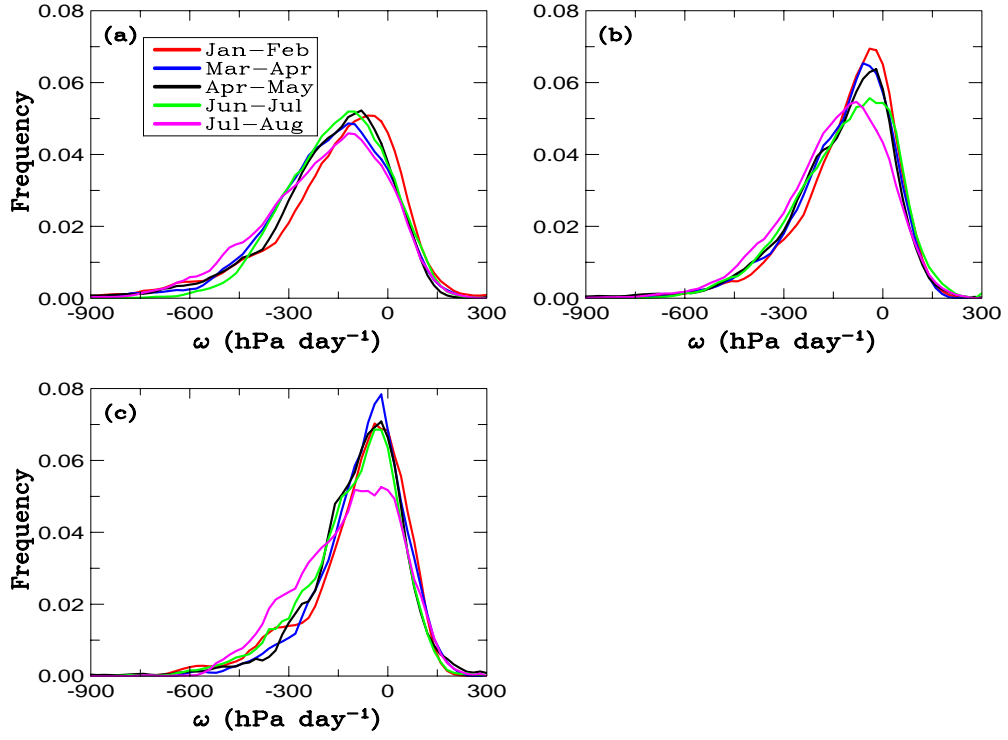
Figure 11: Same as Fig. 7 except for the five precessing cycles.

Table 1: Statistics of the footprint numbers for small-, medium- and large-size categories of cloud objects.

Size category	Mean	Median	Standard deviation	Minimum	Maximum
Small size	114	109	28	76	170
Medium size	344	310	140	171	681
Large size	1535	1233	900	684	7554

Table 2: The *p* values between pairs of size categories for different parameters of tropical convective cloud objects.

Parameter	Between size categories		
	Small, Medium	Medium, Large	Small, Large
SST	0.840	**< 0.001**	**< 0.001**
OLR	**< 0.001**	**< 0.001**	**< 0.001**
Albedo	**< 0.001**	**< 0.001**	**< 0.001**
Cloud height	**< 0.001**	**< 0.001**	**< 0.001**
Cloud temperature	**< 0.001**	**< 0.001**	**< 0.001**
Ice water path	**< 0.001**	**< 0.001**	**< 0.001**
Ice particle size	0.331	**0.044**	0.330
Optical depth	**< 0.001**	**< 0.001**	**< 0.001**

Table 3: Number of cloud objects for small-, medium- and large-size categories as a function of SST ranges. The ratios of large size to all sizes are also shown for the number of cloud objects and the total footprint.

Size category	301.25 K	301.75 K	302.25 K	302.75 K	303.25 K
Small	229	166	194	162	107
Medium	213	170	222	181	113
Large	84	89	114	139	64
Total	526	425	530	482	284
Ratio (number)	0.160	0.209	0.215	0.288	0.225
Ratio (footprint)	0.529	0.625	0.650	0.739	0.675

Table 4: The *p* values between pairs of SST ranges for different parameters of the large-size category of tropical convective cloud objects.

Parameter	Between two SST ranges					
	301.25 K, 301.75 K	301.75 K, 302.25 K	302.25 K, 302.75 K	302.75 K, 303.25 K	301.25 K, 302.75 K	301.25 K, 303.25 K
SST	**< 0.001**	**< 0.001**	**< 0.001**	**< 0.001**	**< 0.001**	**< 0.001**
OLR	0.069	0.826	**0.044**	**0.011**	**0.025**	**< 0.001**
Albedo	0.126	0.734	0.273	0.415	0.577	0.121
Cloud height	**0.004**	0.657	**0.015**	**0.018**	**0.004**	**< 0.001**
Cloud temperature	**0.045**	0.784	0.056	**0.014**	**0.032**	**< 0.001**
Ice water path	0.400	0.817	0.325	0.333	0.343	0.593
Ice particle size	0.825	0.292	0.410	0.526	0.402	0.136
Optical depth	0.869	0.658	0.655	0.635	0.269	0.523

Table 5: Same as Table 4 except for the medium-size category of cloud objects.

Parameter	Between two SST ranges					
	301.25 K, 301.75 K	301.75 K, 302.25 K	302.25 K, 302.75 K	302.75 K, 303.25 K	301.25 K, 302.75 K	301.25 K, 303.25 K
SST	**< 0.001**	**< 0.001**	**< 0.001**	**< 0.001**	**< 0.001**	**< 0.001**
OLR	**0.043**	**0.018**	0.358	**0.047**	**0.007**	**< 0.001**
Albedo	**0.013**	0.508	0.650	0.843	0.876	**0.020**
Cloud height	**0.003**	**0.002**	0.787	0.055	**< 0.001**	**< 0.001**
Cloud temperature	0.057	**0.013**	0.572	**0.048**	**0.006**	**< 0.001**
Ice water path	0.389	0.614	0.241	0.344	0.163	**0.003**
Ice particle size	0.709	0.509	0.300	0.281	0.071	0.055
Optical depth	0.177	0.121	0.707	0.059	0.227	**< 0.001**

Table 6: Same as Table 4 except for the small-size category of cloud objects.

Parameter	Between two SST ranges					
	301.25 K, 301.75 K	301.75 K, 302.25 K	302.25 K, 302.75 K	302.75 K, 303.25 K	301.25 K, 302.75 K	301.25 K, 303.25 K
SST	**< 0.001**	**< 0.001**	**< 0.001**	**< 0.001**	**< 0.001**	**< 0.001**
OLR	0.059	**0.005**	0.263	0.730	**< 0.001**	**< 0.001**
Albedo	0.276	0.881	0.951	0.638	0.948	0.716
Cloud height	**0.001**	**0.001**	0.212	0.820	**< 0.001**	**< 0.001**
Cloud temperature	0.053	**0.004**	0.352	0.485	**< 0.001**	**< 0.001**
Ice water path	0.415	0.194	0.868	0.578	0.174	0.401
Ice particle size	**0.048**	**0.003**	0.942	0.973	**0.013**	0.257
Optical depth	0.756	0.718	0.890	0.765	0.891	0.633

Table 7: Number of observed cloud objects during the five precessing cycles for three cloud object size categories. The cloud object size is in terms of its equivalent diameter. The ratios of large size to all sizes are also shown for the number of cloud objects and the total footprint.

Size category	Jan-Feb	Mar-Apr	Apr-May	Jun-Jul	Jul-Aug
Small	144	170	149	166	187
Medium	163	188	158	154	201
Large	122	90	84	87	96
Total	429	448	391	407	484
Ratio (number)	0.284	0.201	0.216	0.214	0.198
Ratio (footprint)	0.730	0.622	0.676	0.616	0.593

Table 8: The *p* values between pairs of precessing cycles for different parameters of the large-size categories of cloud objects.

Parameter	Between two precessing cycles					
	Jan-Feb, Mar-Apr	Mar-Apr, Apr-May	Apr-May, Jun-Jul	Jun-Jul, Jul-Aug	Mar-Apr, Jun-Jul	Jan-Feb, Jul-Aug
SST	0.688	**0.028**	0.329	**0.006**	**0.004**	**< 0.001**
OLR	0.054	0.070	0.094	0.428	0.081	**0.042**
Albedo	0.781	**0.022**	0.383	0.425	**0.014**	0.151
Cloud height	0.332	0.165	0.561	0.525	0.171	**0.006**
Cloud temperature	0.404	0.058	0.137	0.272	0.119	0.076
Ice water path	0.681	0.114	0.089	0.804	**0.030**	**0.048**
Ice particle size	0.436	**0.021**	**0.019**	0.126	**0.040**	**0.045**
Optical depth	0.686	**0.030**	0.447	0.617	**0.002**	0.069

Table 9: Same as Table 8 except for the medium-size categories of cloud objects.

Parameter	Between two precessing cycles					
	Jan-Feb, Mar-Apr	Mar-Apr, Apr-May	Apr-May, Jun-Jul	Jun-Jul, Jul-Aug	Mar-Apr, Jun-Jul	Jan-Feb, Jul-Aug
SST	0.165	0.431	**0.004**	0.060	**< 0.001**	**< 0.001**
OLR	0.279	**0.003**	**< 0.001**	0.389	0.089	0.139
Albedo	0.141	0.557	0.125	0.478	0.376	**0.020**
Cloud height	0.210	**0.001**	0.055	0.311	0.133	0.215
Cloud temperature	0.065	**0.001**	**0.001**	0.282	0.173	**0.021**
Ice water path	0.315	0.125	0.119	0.061	0.156	**0.015**
Ice particle size	0.253	**0.013**	0.378	**0.010**	**< 0.001**	0.631
Optical depth	0.670	0.762	0.052	0.354	**0.044**	**0.034**

Table 10: Same as Table 8 except for the small-size category of cloud objects.

Parameter	Between two precessing cycles					
	Jan-Feb, Mar-Apr	Mar-Apr, Apr-May	Apr-May, Jun-Jul	Jun-Jul, Jul-Aug	Mar-Apr, Jun-Jul	Jan-Feb, Jul-Aug
SST	0.114	0.314	0.286	**0.022**	**0.008**	**< 0.001**
OLR	0.200	0.357	0.259	**0.047**	**0.007**	0.223
Albedo	0.859	0.662	0.874	0.217	0.437	**0.020**
Cloud height	0.614	0.577	0.418	**0.027**	**0.041**	0.142
Cloud temperature	0.631	0.340	0.317	**0.027**	**0.007**	0.147
Ice water path	**0.038**	0.215	0.785	0.089	0.281	**0.007**
Ice particle size	**0.020**	**0.024**	0.524	0.301	**0.020**	0.213
Optical depth	0.693	0.602	0.650	0.154	0.159	**0.007**